Communication—A Fast and Accurate Numerical Technique for Impedance Spectroscopy of Microstructures

Journal of The Electrochemical Society, 2022 **169** 020543

Communication—A Fast and Accurate Numerical Technique for Impedance Spectroscopy of Microstructures

Narasimhan Swaminathan,[1,z] Sundararajan Natarajan,[1] and Ean Tat Ooi[2]

[1]*Department of Mechanical Engineering, Indian Institute of Technology, Madras, Chennai, 600036, India*
[2]*School of Engineering, Information Technology and Physical Sciences, Federation University, Ballarat, Australia*

The polygonal finite element method (PFEM) is proposed as a fast and accurate technique to simulate the impedance spectroscopy (IS) of polycrystalline materials. While conventional finite element method (FEM) requires explicit meshing of the grains and grain boundaries, in PFEM each region can be treated as an element. We demonstrate that the number of degrees of freedom in PFEM can be lower by a factor of 30 when compared to FEM, thus speeding up simulations by a factor of 3.5. A simple example demonstrates the use of PFEM to generate IS on samples with various grain boundary widths.

 [DOI: 10.1149/1945-7111/ac51a2]

Manuscript submitted November 6, 2021; revised manuscript received January 24, 2022. Published February 16, 2022.

Supplementary material for this article is available online

Impedance spectroscopy (IS) is an experimental technique for materials characterization. IS is used to quantify the contributions of various constituents of a given heterogeneous system to its electrical behavior[1] and to understand mechanisms of surface reactions, kinetics of reactions and mass transport.[2] In materials science the contributions of the grain (bulk), grain boundaries, precipitates or other second phase particles, to the overall electrical response of a given polycrystalline sample[3–5] is often determined using IS. The Nyquist plot generated can provide useful information on the overall resistance or capacitance values. With some understanding of the actual physical processes that occur in the system, meaningful equivalent circuits are generated that reproduce the Nyquist plot. When the electrical response of the system can be idealized as an equivalent circuit with a resistor and a capacitor in parallel, the Nyquist plot is a semi-circle. When such an idealization is not possible, the Nyquist plot may show additional features.[6]

In the context of solid electrolytes, bricklayer models have been used to quantify the conductivities of the grain boundaries, grain-bulk and the role of electrode-current collectors.[7,8] These models neglect actual grain shapes and other inhomogeneities and are useful only for micro-sized grains and homogeneous grain boundary types.[9]

Molecular dynamics simulations can predict the grain-core and grain-boundary conductivities of ion conducting electroceramics.[10,11] These conductivities are often anisotropic and depend on temperature or doping. Grain boundary conductivities also depend on the type (high-angle vs low-angle)[12] and other impurities which may segregate there. Hence, the overall response of the material depends strongly on the microstructure. It has now become necessary to predict the average electrical response of polycrystalline samples when conductivities of various elements of the microstructure are known. This capability will enable design of electroceramics with microstructural features such as grain orientations, grain boundary thickness and types, which can provide favorable electrical response depending on the application. The favorable microstructure may have a certain grain size distribution, or orientation. The grain-widths, grain-type or other dopants may also contribute to the average response of the material.[13] In such cases, obtaining IS data (experimentally) by varying each design parameter is difficult.

Computational methods can be used to obtain IS and evaluate average material responses. Conventional finite element method (FEM) has been used to solve spatio-temporal Maxwell's equations to generate the IS of polycrystalline samples.[14] Reference 15 uses FEM to predict the current density distribution within the sample to identify regions contributing to high impedance. Similar ideas were used in[16] to understand the role of porosity on the electrical properties of $BaTiO_3$. In Ref. 17 the authors show that an increase in amplitude of roughness of the ceramic/electrode interface in multilayer ceramic composites can result in four times increase in electric field strength.

While FEM is often the method of choice for many computational studies, it requires a properly constructed and conforming mesh of the domain.[18] Typical element shapes include triangles/quadrilaterals in 2D and tetrahedra/hexahedra in 3D. Besides requiring a discretization of the grain, a fine mesh is often needed in regions of suspected high gradients (such as grain boundaries) to accurately capture the solution. In the context of solving differential equations over microstructures with large grains and comparatively smaller grain boundaries, a significant effort might be needed to ensure that the element sizes are small enough to capture the gradients in the current densities or the electric field. Often, this requirement increases the number of degrees of freedom. For instance, to model a cubic sample of dimension of 1 μm, the authors used 250,000 tetrahedron prism elements in Ref. 14.

The polygonal finite element method (PFEM),[19–21] has evolved as a versatile method to solve differential equations. One of the main advantages of PFEM over FEM is that elements of arbitrary shapes can be used to discretize the domain. This feature is particularly advantages for computational samples of polycrystalline materials as any polygonal region (like the grain) can be treated as one single element (polygonal). This aspect of treating one grain as a single element is expected to substantially decrease the number of degrees of freedom with only a marginal sacrifice in accuracy.

We demonstrate the applicability of PFEM to generate IS for polycrystalline samples. The accuracy and speed of PFEM is demonstrated by comparing the results with FEM. We then show using a simple example how PFEM can be used to examine the variation of IS with grain boundary widths. A more involved example which uses a polycrystalline sample with grain boundaries having anisotropic conductivities is demonstrated in the Supplementary Material.

Theoretical Formulation

We follow Ref. 14 and consider the differential form of Maxwell's continuity equation:

$$\frac{\partial \rho}{\partial t} + \nabla \cdot J = \frac{\partial \rho}{\partial t} + \nabla \cdot (J_c + J_d) = 0 \qquad [1]$$

where J is the total current density and ρ the charge density. $J_c = \sigma E$, is the differential form of Ohm's law, $J_d = \frac{\partial D}{\partial t}$ is the

[z]E-mail: n.swaminathan@iitm.ac.in

displacement current density, σ is the conductivity, E is the electric field and D is the electric displacement.

E and the electric potential ϕ are related by:

$$E = -\nabla\phi \quad [2]$$

D is related to E through

$$D(x, t) = \varepsilon(x)E(x, t) \quad [3]$$

As no time dispersion is considered, the electric permittivity $\varepsilon(x)$ is only a function of space. Using Eqs. 2–3, we transform Eq. 1 to

$$-\nabla\cdot\left[\sigma(x)\nabla\phi(x, t) + \varepsilon(x)\frac{\partial}{\partial t}\nabla\phi(x, t)\right] = 0 \quad [4]$$

The corresponding weak form of Eq. 4 is: Find $\phi \in U$ such that

$$\begin{aligned}\forall\ \delta\phi \in V,\ &\int_\Omega \nabla\delta\phi\sigma(x)\nabla\phi(x, t)d\Omega \\ &+ \int_\Omega \nabla\delta\phi\varepsilon(x)\frac{\partial}{\partial t}\nabla\phi(x, t)d\Omega \\ &= \int_{\partial\Omega} \delta\phi\sigma(x)\nabla\phi(x, t)d\Omega\end{aligned} \quad [5]$$

where U and V are the trial and test spaces that include linear fields.

In a routine way, the domain may be partitioned into non-overlapping elements, ϕ^h and on using shape functions N_a that span at least the linear space, we substitute the trial and test functions $\phi^h = \sum_a N_a\phi_a$ and $\delta\phi^h = \sum_b N_b\delta\phi_b$, respectively, into Eq. 5 to obtain the space discretized weak form:

$$\begin{aligned}\forall\ \delta\phi^h \in V,\ &\int_\Omega \nabla\delta\phi^h\sigma(x)\nabla\phi^h(x, t)d\Omega \\ &+ \int_\Omega \nabla\delta\phi^h\varepsilon(x)\frac{\partial}{\partial t}\nabla\phi^h(x, t)d\Omega \\ &\times \int_{\partial\Omega} \delta\phi^h\sigma(x)\nabla\phi^h(x, t)d\Omega\end{aligned} \quad [6]$$

In FEM, the grains/grain boundaries must be discretized and material properties (σ), should be assigned to each element. In the PFEM approach, each grain core and grain boundary regions are each idealized as one single finite element, naturally reducing the number of unknowns in the problem.

Polygonal finite element method—Overview.—PFEM and FEM differ in the manner the trial (or test) functions are constructed. PFEM is a generalization of FEM that allows for arbitrary element shapes and sizes. The test functions in PFEM must satisfy partition of unity, interpolation, linear completeness and non-negativity. There is no unique way to represent the trial functions with these properties over arbitrary polytopes.[22–29] Wachspress,[22] mean-value coordinates,[24] Laplace interpolants,[23,25] Harmonic coordinates,[26–28] are a few approaches to generate such functions (See Ref. 29). Mean-value coordinates (Floater[24]) are used here as they work efficiently for both convex and concave regions. The mean value coordinates for a point, $P(x)$ in an arbitrary polygon is given by:

$$N_a(x) = \frac{w_I(x)}{\sum_{J=1}^{n} w_J(x)} \quad [7]$$

where

$$w_I(x) = \frac{\tan(\alpha_{I-1}/2) + \tan(\alpha_I/2)}{\vee x - x_I \vee} \quad [8]$$

where n is the number of nodes in an element, x_I is the coordinate of the point P_I and α_I's are the internal angles (See Fig. 1 of Ref. 24). N_a over arbitrary shaped polygons are rational functions and integration rules and evaluation of derivatives to calculate Eq. 5 are not as clear as evidenced by growing literature on this aspect.[30–33] A sub-triangulation of the polygonal domain is employed in this work, and integrals are evaluated at Gauss-quadrature points of these triangles.

Simulation Details

All simulations were conducted using MATLAB 2020a. Simulations to compare FEM and PFEM were conducted on quad core Intel i7-@2.8 GHz with 16 GB RAM, with identical parallelization for the assembly of the stiffness matrix.

Details of the microstructure.—A square domain with side $l =$ 300 nm was used to create a two-dimensional microstructure. Each grain was generated from circles of radius $\cong 2$ nm amounting to about 80 grains. Four grain boundary widths, $\Delta W = 1, 2, 3$ and 4 nm were considered for the study. The top boundary was extended by 3 nm and this region was assumed to be highly conductive material to simulate a metallic contact. The microstructure was generated by modifying the *microstructpy*[34] package. This microstructure is then altered by shrinking the grains by an appropriate amount related to

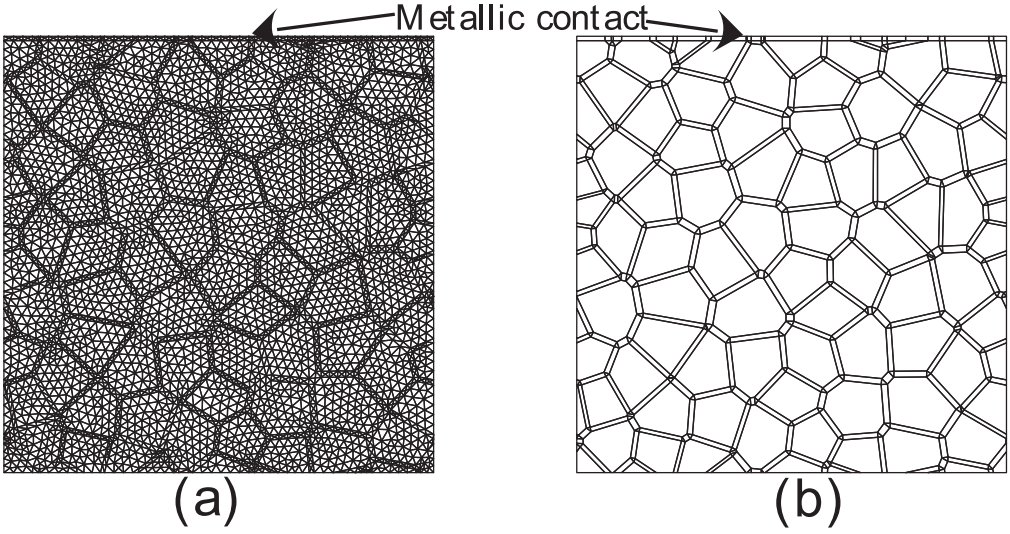

Figure 1. Polycrystalline domain (a) finite element mesh with 8128 elements and 4181 nodes and (b) PFEM with 516 elements and 574 nodes including grain and grain boundary regions.

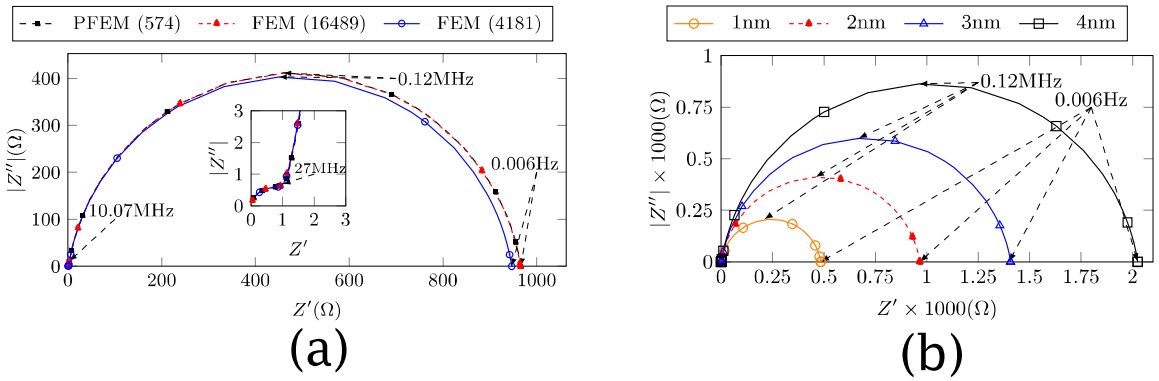

Figure 2. (a) Nyquist plot for the sample in Fig. 1 comparing FEM and PFEM results. The numbers within ( ) indicate the number of nodes in the sample (b): Nyquist plots for various grain boundary widths. It is clearly seen that the resistance increases drastically with small increases in the grain boundary widths. These results were generated using PFEM with 78 grains and contains 574 degrees of freedom.

ΔW to create grain boundary domains. The created grain boundary domains are further meshed for FEM or PFEM.

Material properties.—The conductivities of the grain core σ_{gc}, grain boundary σ_{gb} and the metallic region σ_m were 100×10^{-2} S m^{-1}, 100×10^{-6} S m^{-1} and 10×10^{3} S m^{-1}, respectively. The permittivity of all regions is assumed to be a constant with a relative permittivity $\varepsilon_r = 100$. The impedances were sampled in the range 0.001 Hz to 1 GHz.

Finite element mesh.—For FEM simulations two meshes with triangular elements having 4,181 nodes and 16,489 nodes (Fig. 1a), were considered. For PFEM, the vertices of the grains or grain boundaries were the only nodes required (See Fig. 1b).

Simulation procedure.—Five cycles of a sinusoidal Voltage (V) of magnitude 100 V were applied at the metallic end of the microstructure, while the other sides were insulated. Ordinary differential equations arising from the FEM or PFEM were numerically integrated in time using an implicit scheme with a time step $\Delta t = \frac{1}{20\omega}$, where ω is the frequency in Hz. At each time step, the current (I) at the metallic ends was calculated and accumulated. For each ω, the phase difference $\Delta\varphi$ between V and I is obtained using Fast Fourier Transforms. The imaginary (Z″) and real (Z′) parts of the impedance are computed as Rsin($\Delta\phi$) and Rcos ($\Delta\phi$), respectively, where R is the ratio of the amplitudes of V and I. The left and right sides were insulated and the potential φ at the metallic end is measured with respect to the lower side of the sample.

Results and Discussion

Comparison with the regular finite element method (FEM).—Figure 2a shows the Nyquist plot and the inset shows the high frequency response. Figures S2a–S2d (available online at stacks.iop.org/JES/169/020543/mmedia) compares the current densities between the two methods for two frequencies. It is very clear that the results obtained from PFEM and that of FEM (with 16,489 nodes) match perfectly, in both high and low frequency regimes. For low frequencies, the coarser finite element mesh with nearly eight times the nodes as that of PFEM shows an inferior performance. Furthermore, the time taken for completing the simulation for PFEM (574 nodes) was ≅20 s, while that for the FEM (16,489 nodes) was ≅70 s. Clearly, PFEM is an effective method to study impedance spectroscopy of microstructures.

Examples.—To demonstrate the use of the proposed PFEM, we consider a simple example of determining the average resistance/capacitance of a microstructure with different grain boundary widths ΔW. Figure 2b shows the Nyquist plots for four different grain boundary widths. The average resistance increases with ΔW, as expected. A small change in ΔW enhances the resistance to a large extent. An additional example that involves role of anisotropic conductivity of the grains and grain boundaries is provided in the Supplementary Material.

Conclusions

Speed, accuracy and robustness of the PFEM over FEM for computational simulation of IS is demonstrated. With the properties of the grain boundaries and grain cores specified, IS simulations can reveal a wealth of information on the average electrical behavior of the microstructure. While samples in this work were taken to be 300 nm, microstructures have several hundreds to thousands of grains with typical dimensions in the order of several hundred microns and each grain being 1–10 μm in diameter. Application of FEM to such a real microstructure with even a reasonable mesh size would be computationally expensive, time consuming and hence prohibitive. PFEM can treat each grain and grain boundary region as a single element and extract useful information on a realistic microstructure with reasonable accuracy in a fraction of the time. With such a tool, the effect of various features of the microstructures can be quickly studied as demonstrated in this work. Such a tool will be very effective in designing/tailoring microstructures within a short time to suit specific applications.

ORCID

Narasimhan Swaminathan https://orcid.org/0000-0001-8572-3766

References

1. A. Bard and L. Faulkner, *Electrochemical Methods: Fundamentals and Applications* (Wiley, New York, NY) (2000).
2. N. O. Laschuk, E. B. Easton, and O. V. Zenkina, *RSC Adv.*, **11**, 27925 (2021).
3. I. Hodge, M. Ingram, and A. West, *J. Electroanal. Chem. Interf. Electrochem.*, **74**, 125 (1976).
4. K. Srinivas, P. Sarah, and S. Suryanarayana, *Bull. Mater. Sci.*, **26**, 247 (2003).
5. D. T. Swamy, K. E. Babu, and V. Veeraiah, *Bull. Mater. Sci.*, **19**, 1115 (2013).
6. E. Abram, D. Sinclair, and A. West, *J. Electroceramics*, **10**, 165 (2003).
7. T. Van Dijk and A. Burggraaf, *Phys. Status Solidi A*, **63**, 229 (1981).
8. X. Guo and R. Waser, *Prog. Mater Sci.*, **51**, 151 (2006).
9. N. Kidner, Z. Homrighaus, B. Ingram, T. Mason, and E. Garboczi, *J. Electroceramics*, **14**, 283 (2005).
10. L. Momenzadeh, I. V. Belova, and G. E. Murch, *Comput. Condens. Matter*, **28**, e00583 (2021).
11. A. R. Symington, M. Molinari, J. A. Dawson, J. M. Statham, J. Purton, P. Canepa, and S. C. Parker, *J. Mater. Chem. A*, **9**, 6487 (2021).
12. A. A. Riet, J. A. Van Orman, and D. J. Lacks, *Geochim. Cosmochim. Acta*, **292**, 203 (2021).
13. E. Van Der Giessen et al., *Model. Simul. Mater. Sci. Eng.*, **28**, 043001 (2020).
14. J. S. Dean, J. H. Harding, and D. C. Sinclair, *J. Am. Ceram. Soc.*, **97**, 885 (2014).
15. J. P. Heath, J. S. Dean, J. H. Harding, and D. C. Sinclair, *J. Am. Ceram. Soc.*, **98**, 1925 (2015).

16. G. Dale, M. Strawhorne, D. C. Sinclair, and J. S. Dean, *J. Am. Ceram. Soc.*, **101**, 1211 (2018).
17. J. P. Heath, J. H. Harding, D. C. Sinclair, and J. S. Dean, *J. Eur. Ceram. Soc.*, **39**, 1170 (2019).
18. O. Zienkiewicz, R. Taylor, R. Taylor, and J. Zhu, *The Finite Element Method: Its Basis and Fundamentals* (Butterworth-Heinemann, Oxford) (2013).
19. G. Manzini, A. Russo, and N. Sukumar, *Math. Models Methods Appl. Sci.*, **24**, 1665 (2014).
20. N. Sukumar, *Int. J. Numer. Methods Eng.*, **61**, 2159 (2004).
21. N. Sukumar, B. Moran, and T. Belytschko, "The natural element method in solid mechanics." *Int. J. Numer. Methods Eng.*, **43**, 839 (1998).
22. E. Wachspress, *Rational Bases and Generalized Barycentrics* (Springer, Berlin) (2016).
23. N. Sukumar and E. Malsch, *Arch. Comput. Methods Eng.*, **13**, 129 (2006).
24. M. S. Floater, *Comput. Aided Geom. Des.*, **20**, 19 (2003).
25. P. Joshi, M. Meyer, T. DeRose, B. Green, and T. Sanocki, *ACM Trans. Graph.*, **26**, 71 (2007).
26. J. Warren, S. Schaefer, A. N. Hirani, and M. Desbrun, *Adv. Comput. Math.*, **27**, 319 (2007).
27. J. E. Bishop, *Int. J. Numer. Methods Eng.*, **97**, 1 (2014).
28. N. Sukumar and A. Tabarraei, *Int. J. Numer. Methods Eng.*, **61**, 2045 (2004).
29. K. Hormann and N. Sukumar (ed.), *Generalized Barycentric Coordinates in Computer Graphics and Computational Mechanics* (CRC Press, Boca Raton, FL) (2017).
30. S. Natarajan, S. P. Bordas, and D. R. Mahapatra, *Int. J. Numer. Methods Eng.*, **80**, 103 (2009).
31. S. Mousavi, H. Xiao, and N. Sukumar, *Int. J. Numer. Methods Eng.*, **82**, 99 (2010).
32. E. B. Chin, J. B. Lasserre, and N. Sukumar, *Comput. Mech.*, **56**, 967 (2015).
33. A. Francis, A. Ortiz-Bernardin, S. P. Bordas, and S. Natarajan, *Int. J. Numer. Methods Eng.*, **109**, 1263 (2017).
34. K. A. Hart and J. J. Rimoli, *SoftwareX*, **12**, 100595 (2020).